CHAPTER-6

Synthesis of Single Phase Ti^{4+} substituted Trirutile $CoNb_2O_6$ Ceramic: Evolution of Relaxor type Ferroelectricity and High k Dielectricity

6.1 INTRODUCTION

The dielectric constant of material ultimately decides the level of miniaturization in electronic devices based on capacitive components and the development of wireless communications technologies operating at microwave frequencies. Among the several niobates that were examined, our primary focus was on $CoNb_2O_6$ because of its potential to act as a high-k relaxor dielectric or ferroelectric. Thermodynamic properties such as entropy, heat capacity, or susceptibility are first detected at the quantum critical point (QCP) in ferroelectrics, where the ferroelectric transition temperature may be tuned down to zero.[1-3] This allows the QCP to be located near the ferroelectric phase transition. Ferroelectric materials may be used in a variety of applications, including tunable phase shifters, capacitors, DRAMs, memory devices, oscillators, and infrared detectors for use in navigation and security systems.[4-8]

In this chapter, the study was to create a novel lead-free high-k relaxor dielectric that has the potential for great performance as well as a high Curie temperature. Ti^{4+} substitution on the Nb site in $CoNb_2O_6$ was contemplated in this study to develop innovative high k dielectric/ferroelectric properties as a result of decreased oxidation. Both smaller cations (Co^{3+} and Ti^{4+}) can lead to net dipole moment in each octahedron from the deviation from the mean position in octahedra and can generate high k dielectricity or it may turn the material into lead-free ferroelectricity. Ti^{4+} cation can lead to oxidation of Co^{2+} ion into Co^{3+} in rigid Trirutile octahedral network. In the system that was created via the traditional solid-state reaction and sintering approach, two different compositions $CoNb_{1.95}Ti_{0.05}O_6$ and $CoNb_{1.9}Ti_{0.1}O_6$ were studied. A clear P-E loop was seen for the sample, which hints at the presence of ferroelectric-type behavior in the material. The behavior of the relaxor

dielectric characteristic of the material was analyzed here, and the results showed relaxor dielectric and ferroelectric-type activity.

6.2 Material Synthesis and Characterizations

In this chapter Ceramic samples of $CoNb_{2-x}Ti_xO_6$ were generated using a modified solid-state approach in the range of x = 0.05 to 0.1 in the molar ratio, 1: 2-x: x. This was done in the range of x = 0.05 to 0.1. In an agate mortar, 10 mmol of $CoCO_3$, 9.75 mmol of Nb_2O_5, and 0.5 mmol of TiO_2 were manually mixed to produce $CoNb_{1.95}Ti_{0.05}O_6$, and 10 mmol of $CoCO_3$, 9.5 mmol of Nb_2O_5, and 1 mmol of TiO_2 were used to produce $CoNb_{1.9}Ti_{0.1}O_6$. The samples were then calcined. To do this, samples were allowed to heat up to 1200 ^oC for six hours before being put on hold for another 15 hours. After that, we allowed the temperature to return to normal temperature through natural cooling.

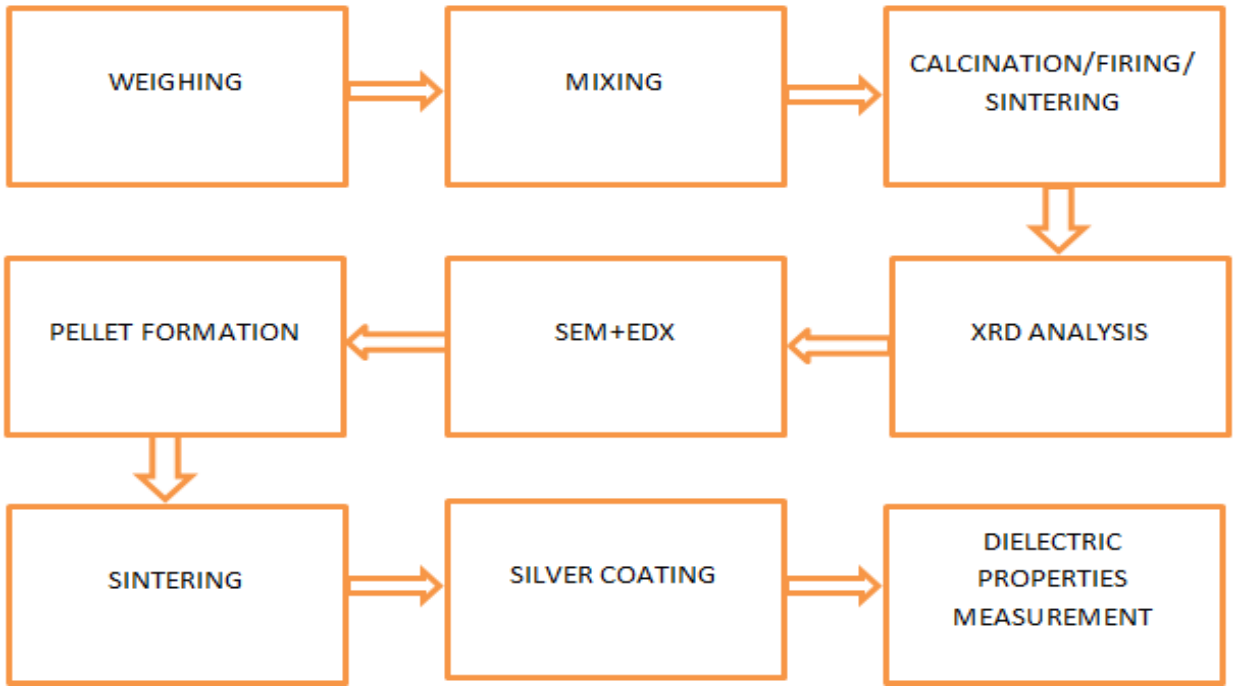

Figure 6.1 Schematic of the synthesis scheme of $CoNb_2O_6$ and $CoNb_{2-x}Ti_xO_6$ ceramic samples.

Powder x-ray diffraction (XRD) examination was used to investigate the samples of $CoNb_2O_6$ and $CoNb_{2-x}Ti_xO_6$ to determine their structures as well as the phase purity of the compounds. For the XRD, a RIGAKU diffractometer (Smart Lab 9KW, Target: Cu Kα, λ=1.5408Å) was used. The Rietveld technique was used to refine the structure of the samples, and the orthorhombic structure of $CoNb_2O_6$ was utilized as the model structure. Using scanning electron microscopy, an examination of the microstructure of the sintered pellets was carried out. To validate the material's chemical composition, an EDX analysis was carried out using the probe that was attached to the SEM apparatus(EVO-18 Research, ZEISS). Studies using X-ray Photoelectron Spectroscopy (XPS) have been carried out to investigate the electronic structure of the materials by Thermo Scientific Multilab 2000 by using Al K at a power output of 150 W. The binding energies that have been presented here are correct to within 0.1 eV, and they are calculated with reference to C (1s) at 284.5 eV. After that, we used emery paper with a fine grain size to polish the pellet, and then we treated it at a temperature of 600 ^oC to eliminate any residual stresses present in the pellet. After that, we did electroding by silver paste on both sides of the pellet. Then we dried it out by heating it at 400 ^oC for an hour to cure the pellets. A Metrohm Autolab (PGSTAT204) fitted with an FRA32M module was used to conduct the complicated impedance spectroscopy analysis of $CoNb_{2-x}Ti_xO_6$ pellets. The NOVA program was used to analyze the impedance data. The measurements of the two-probe AC impedance were carried out in the air throughout a frequency range of 100 Hz to 100 kHz, and an applied AC amplitude of 20 mV was used for each experiment. The RADIANT precision premier II instrument was used to conduct ferroelectric measurements at room temperature with a range of applied voltages from 10 kV to 50 kV and a frequency of 50 Hz.

6.3 Structural Study

Powder X-ray diffraction patterns have been used to investigate the structural characteristics as well as the phase purity. Figure 6.2(a) displays the XRD patterns of $CoNb_2O_6$ and $CoNb_{2-x}Ti_xO_6$, respectively. The crystallinity of all of the samples is shown by diffraction patterns that are distinct and sharp peaks for each sample. In addition to this, it demonstrates an impurity-free sample of a clean orthorhombic phase (s.g. Pbcn), in the Trirutile structure. This is applicable over the whole doping range. The Rietveld approach was used to get a more precise understanding of the structure of the materials while using the FullProf software. The Rietveld refined XRD picture of the $CoNb_2O_6$ phase as well as the $CoNb_{2-x}Ti_xO_6$ phase can be seen in Figure 6.2(b), (c), and (d) respectively.

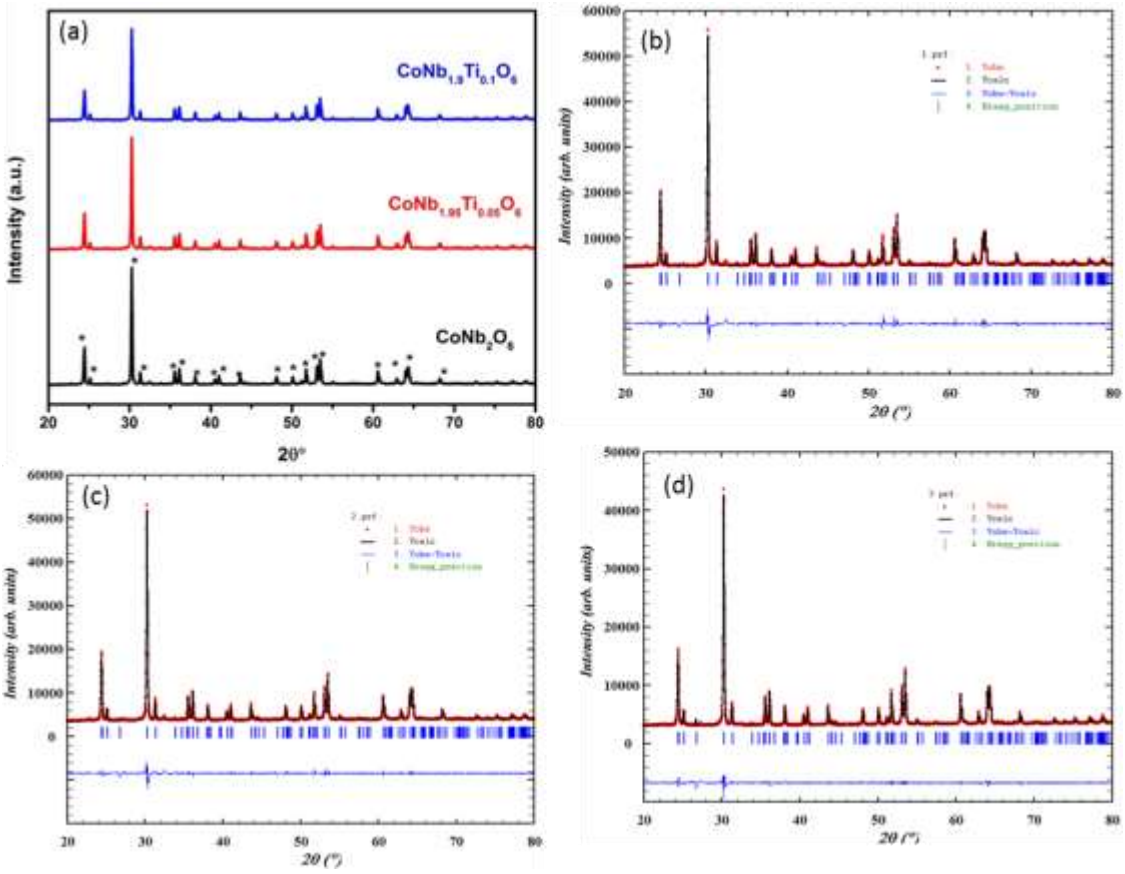

Figure 6.2: (a) Powder XRD pattern of $CoNb_2O_6$, $CoNb_{1.95}Ti_{0.05}O_6$, and $CoNb_{1.9}Ti_{0.1}O_6$ ceramic samples. (b) Rietveld refined powder XRD pattern of $CoNb_2O_6$ (c) Rietveld refined powder XRD pattern of $CoNb_{1.95}Ti_{0.05}O_6$ and (d) Rietveld refined powder XRD pattern of $CoNb_{1.9}Ti_{0.1}O_6$.

The lack of diffraction peaks for metallic Ti and TiO_2 phases, or the presence of a minor quantity of them, shows that Ti may have been substituted for Nb in the $CoNb_2O_6$ lattice without affecting the structure of the compound. The following table (Table 6.1) presents the structural characteristics that were determined from Rietveld refinements of $CoNb_2O_6$ and $CoNb_{2-x}Ti_xO_6$ (x = 0.05, 0.1). There is hardly any discernible shift seen in the lattice characteristics of $CoNb_{2-x}Ti_xO_6$. However, when the amount of Ti that is doped into the powder increases (x > 0.1), weak diffraction peaks that correspond to the rutile TiO_2 phase begin to show in the powder XRD pattern. This is because the Ti ions begin to segregate into their respective phases. Therefore, only a maximum of 10% of the $CoNb_2O_6$ lattice may have Ti ions replaced for Nb ions.

Table 6.1. Structural Parameters of $CoNb_2O_6$, $CoNb_{1.95}Ti_{0.05}O_6$, and $CoNb_{1.9}Ti_{0.1}O_6$.

Compound	Lattice Parameters (Å)			χ^2	R_f	R_{Bragg}	R_{wp}
	a	b	c				
$CoNb_2O_6$	14.1699(2)	5.7079(2)	5.0475(1)	1.703	2.65	2.79	13.7
$CoNb_{1.95}Ti_{0.05}O_6$	14.1694(1)	5.7105(3)	5.0475(3)	1.951	1.49	1.52	12.1
$CoNb_{1.9}Ti_{0.1}O_6$	14.1680(3)	5.7122(1)	5.0469(2)	1.476	1.13	1.17	10.4

6.4 SEM/EDAX Study

Figures 6.3(a), 6.4(a), and 6.5(a) show scanning electron micrographs of the powder of $CoNb_2O_6$ and pellets of $CoNb_{1.95}Ti_{0.5}O_6$ and $CoNb_{1.95}Ti_{0.5}O_6$, respectively. According to the results of the SEM image, the grains for the powder sample have diameters ranging from 5 to 25 micrometers and have an orthorhombic form. Images captured by an SEM show a dense pellet that is devoid of porosity and voids at the surface. The EDX pictures for the powder of $CoNb_2O_6$ and pellets of $CoNb_{1.95}Ti_{0.5}O_6$ and $CoNb_{1.95}Ti_{0.5}O_6$ also validate the composition of the materials. These images are

shown in Figures 6.3(b), 6.4(b), and 6.5(b) respectively. The Archimedes technique was used to determine the density of the pellets in water, and the results showed that the pellets had a density that was about 97% of the material's theoretical density.

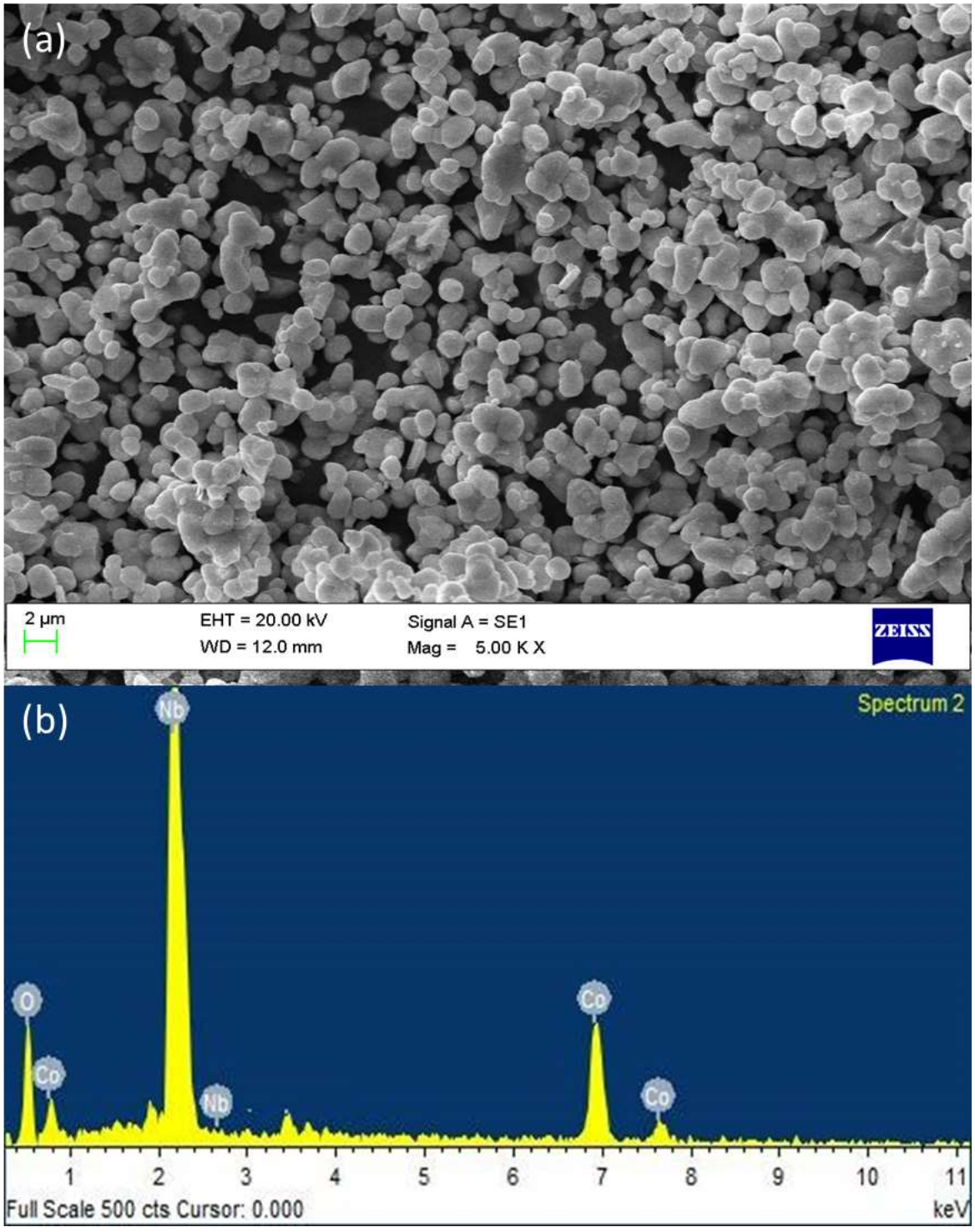

Figure 6.3: (a) SEM image and (b) EDAX of $CoNb_2O_6$ powder sample.

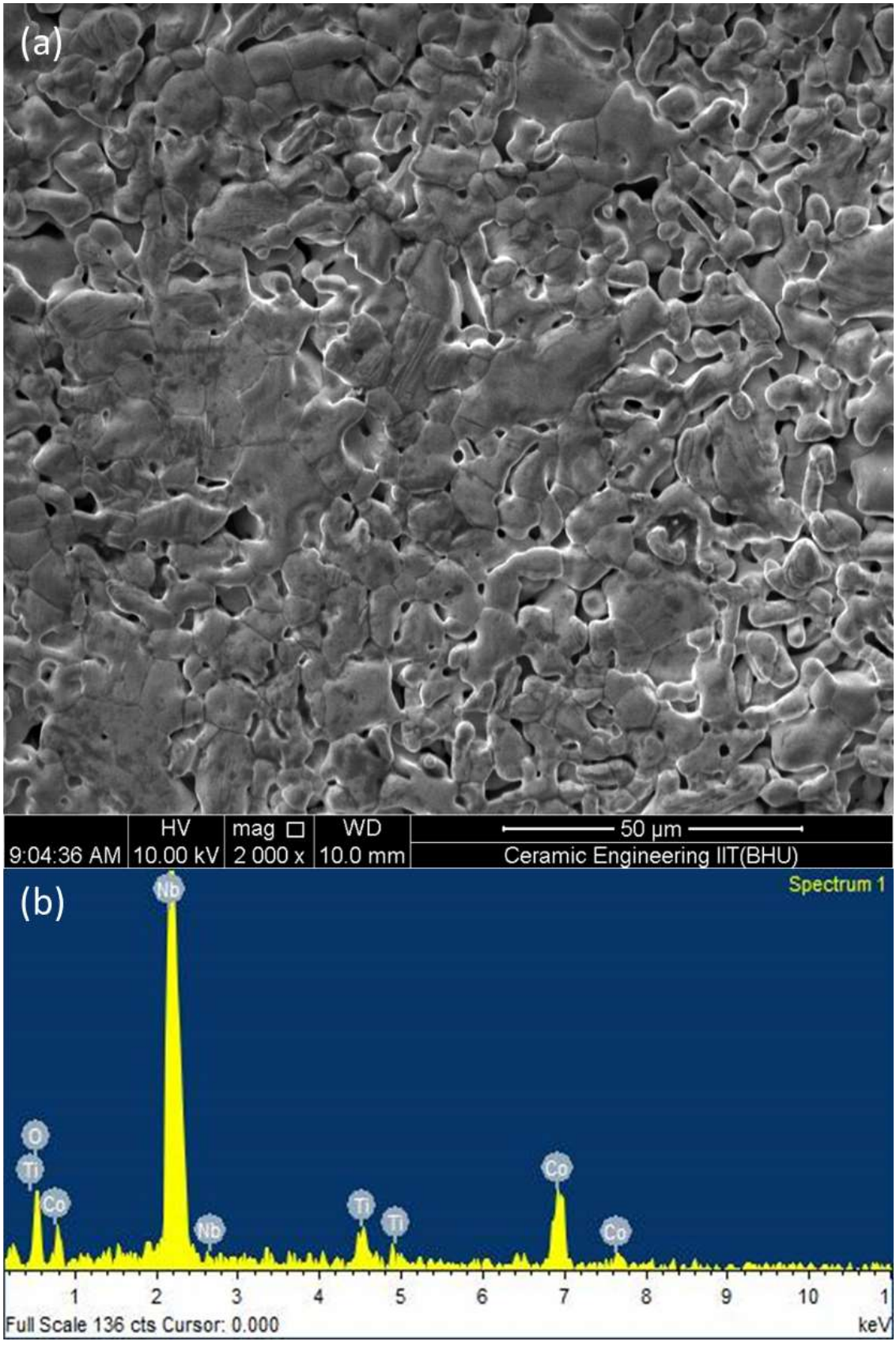

Figure 6.4: (a) SEM image and (b) EDAX of the sintered ceramic pellet of $CoNb_{1.95}Ti_{0.05}O_6$ sample.

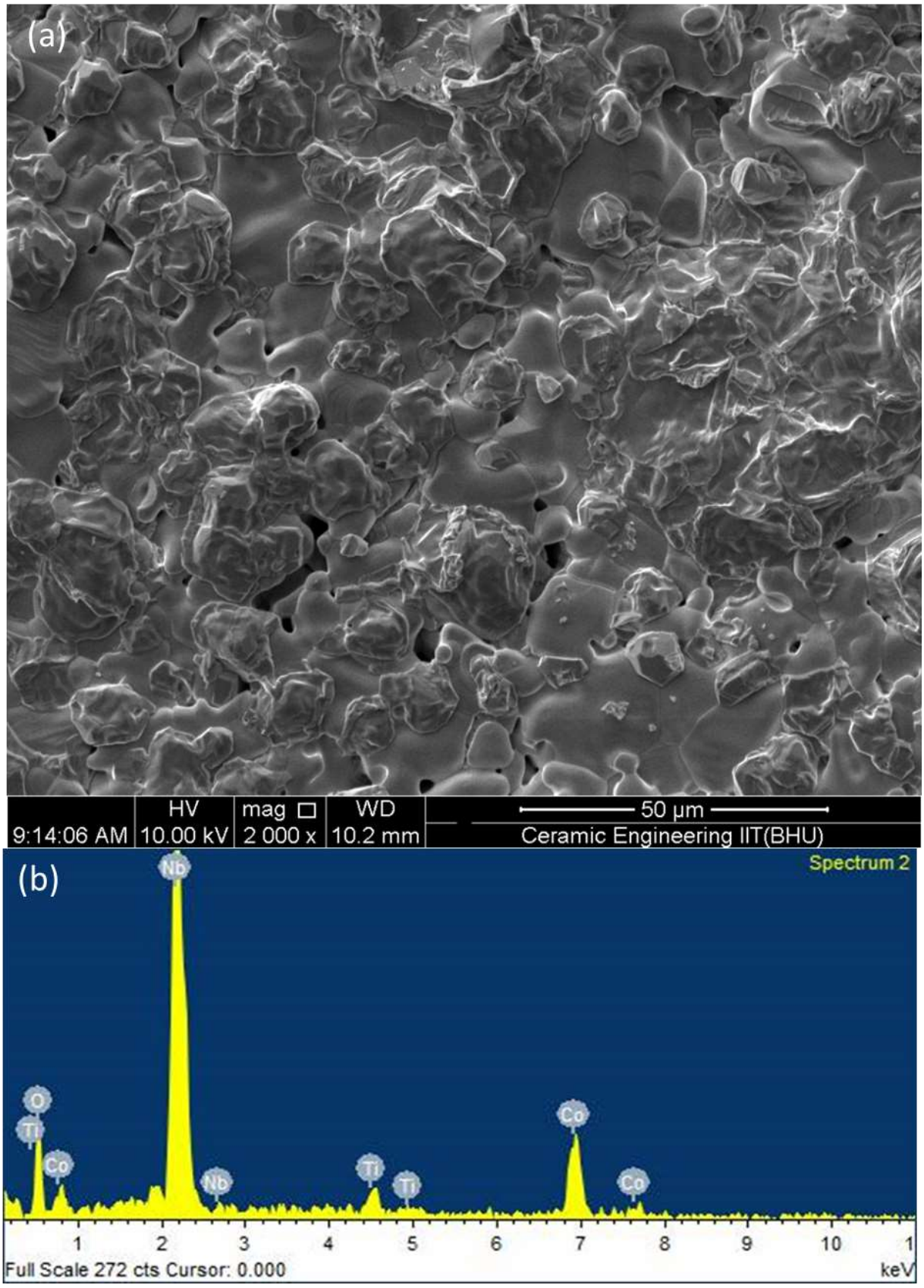

Figure 6.5: (a) SEM image and (b) EDAX of the sintered ceramic pellet of $CoNb_{1.9}Ti_{0.1}O_6$ sample.

6.5 XPS Study

X-ray photoelectron spectroscopy was used to look into the electronic structure of the samples of $CoNb_{1.9}Ti_{0.1}O_6$ as well as the oxidation states. The survey spectra obtained from the XPS analysis of the $CoNb_{1.9}Ti_{0.1}O_6$ pellets are shown in Figure. 6.6(a). Figure 6.6(b) displays the core level Co(2p) spectrum that was obtained from the $CoNb_{1.9}Ti_{0.1}O_6$ sample. Peaks attributed to 2p3/2 at 779.1 eV and 2p1/2 at 794.8 eV, together with fused satellite peaks, belong to Co^{3+} ions. The 2p3/2 and 2p1/2 peaks designated at 779.85 eV and 794.9 eV, respectively, correspond to Co^{2+} ions, as does the strong satellite peak at 785.8 eV and 802.4 eV. The ratio of the Co^{2+} ions to the Co^{3+} ions that were discovered in the sample was determined based on their peak intensity. The ratio of the Co^{2+} ions to the Co^{3+} ions that were found in the sample that was composed of $CoNb_{1.9}Ti_{0.1}O_6$ was found to be 89:11. This proves that the replacement of Ti^{4+} ions on Nb^{5+} sites in the $CoNb_2O_6$ lattice causes Co^{2+} to be oxidized into Co^{3+} to maintain the charge neutrality in the lattice. This is necessary since a rigid Trirutile lattice cannot accept a lattice oxygen vacancy. The Spectra of the core level Nb(3d) can be seen in Figure. 6.6(c), which depicts the $CoNb_{1.9}Ti_{0.1}O_6$ sample. There was no satellite peak present, which indicates that the Nb^{5+} oxidation state was present in the sample. The binding energy of Nb(3d3/2) was measured at 205.9 eV, while Nb(3d5/2) was measured at 208.9 eV. Ti(2p1/2) blended with Nb(3s) spectra, which resulted in a wide range of spectra being shown in Figure. 6.6(d). The binding energy of the Ti(2p3/2) complex was measured to be 457.8 eV. The O(1s) spectra may be deconvoluted into two distinguishable peaks: (1) the lattice oxygen species peak at 530.5eV and (2) the adsorb wide oxygen peak at about 531.2 eV for hydroxide or absorbed moisture on the surface. Both of these peaks are located at the same energy level.

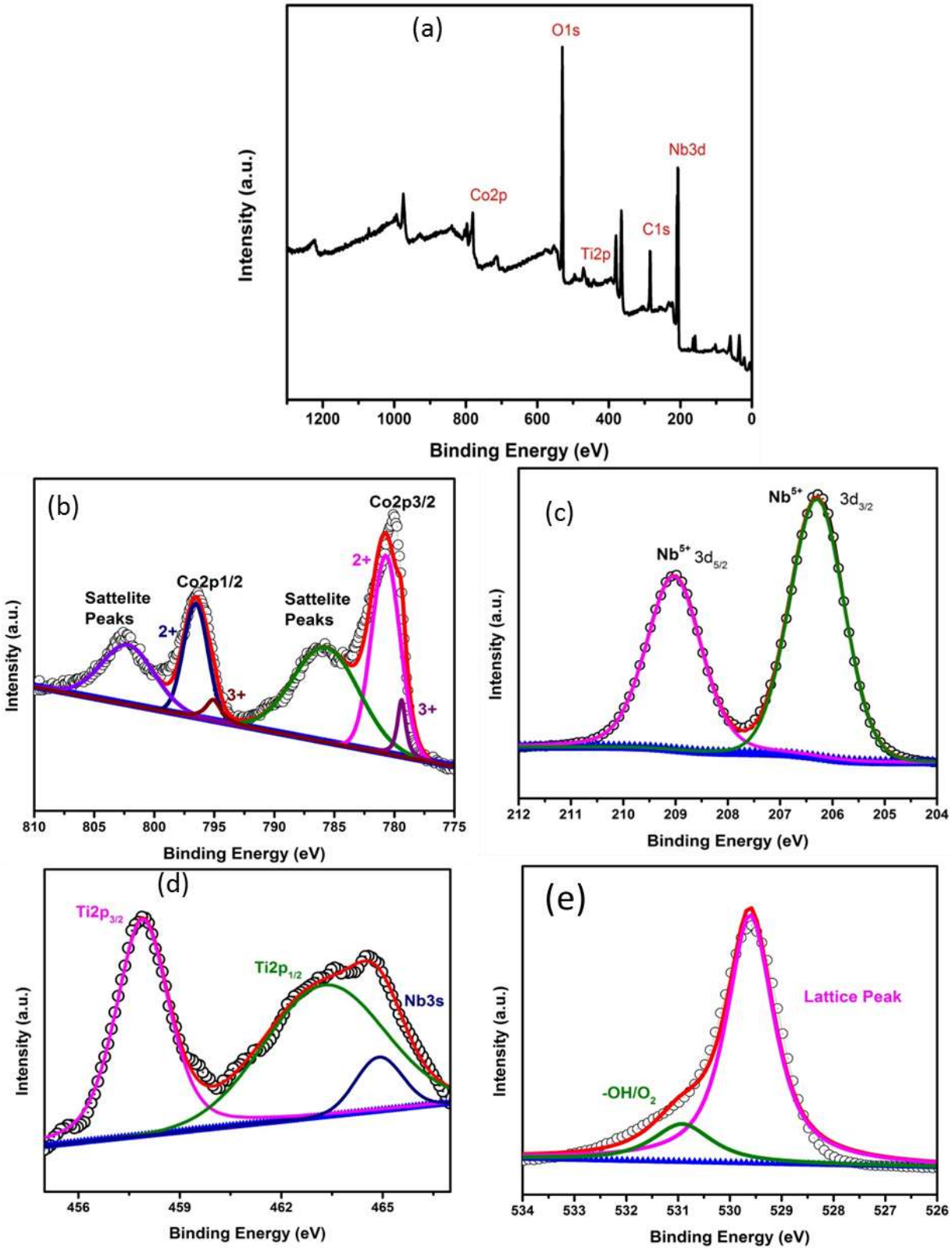

Figure.6.6: XPS of $CoNb_{1.9}Ti_{0.1}O_6$ (a) Full survey, (b) Core level of Co(2p), (c) Core level of Nb(3d), (d) Core level of Ti(2p), (e) Core level of O(1s).

6.6 Dielectric Study

To investigate how the material behaved dielectrically across the frequency range of 100 kHz to 100 Hz using impedance spectroscopy, the procedure had to be performed in air at varying temperatures. The formula that was used to compute the dielectric constant is as follows:

$$\varepsilon_r = \frac{C*d}{\varepsilon_\circ * A} \tag{6.1}$$

Where; ε_r is the dielectric constant, C is capacitance, ε_o is the permittivity of free space ($8.85*10^{-12}$)F/m, d is the thickness of the pellet, A is the area of the pellet;

Capacitance (C) was calculated using the formula

$$C = -\frac{1}{\omega}\left[\frac{Z''}{Z'^2 + Z''^2}\right] \tag{6.2}$$

and the dielectric loss was calculated by using the formula

$$\tan\delta = \frac{\varepsilon''}{\varepsilon'} = \frac{Z'}{-Z''} \tag{6.3}$$

Plots of the real part of the dielectric constant for the $CoNb_2O_6$, $CoNb_{1.95}Ti_{0.05}O_6$, and $CoNb_{1.9}Ti_{0.1}O_6$ pellets are shown in figures 6.7(a), 6.8(a), and 6.9(a), respectively, for the frequency range of 100 Hz to 100 kHz. The temperature range for these plots is from room temperature to 400. The $\varepsilon_{r'}$ values, in general, increase as the temperature increases, with the highest values reaching their maximums at about 200 ^oC at all frequencies. The maximum value decreases after 200 ^oC and shows the relaxor-type phenomena. The dielectric constant was determined to be 500 for $CoNb_2O_6$, 700 for $CoNb_{1.95}Ti_{0.05}O_6$, and 14000 for $CoNb_{1.9}Ti_{0.1}O_6$ respectively. The values of dielectric

constant decrease with an increase in frequency clearly showing the behavior of relaxor type at 200 ^{o}C for $CoNb_{1.95}Ti_{0.05}O_6$, and $CoNb_{1.9}Ti_{0.1}O_6$ and 250 ^{o}C for $CoNb_2O_6$. Figures 6.7(b), 6.8(b), and 6.9(b) illustrate the fluctuation in dielectric loss with the temperature at the same frequency range. Taking into account the high dielectric constant of the materials, the reported dielectric loss in the $CoNb_2O_6$, $CoNb_{1.95}Ti_{0.05}O_6$, and $CoNb_{1.9}Ti_{0.1}O_6$ samples is much lower. Nevertheless, when the frequency was increased, both the dielectric constant and the dielectric loss were found to be reduced. It is likely that the localized nature of hopping charge carriers, in addition to interfacial polarization due to space charge, is responsible for the increase in dielectric constant that occurs with increasing temperatures at different frequencies for $CoNb_2O_6$, $CoNb_{1.95}Ti_{0.05}O_6$, and $CoNb_{1.9}Ti_{0.1}O_6$. Due to the vibration of the Ti^{4+} cation from its mean position in the octahedral, which may result in net polarization or a dipole moment in the octahedral, the replacement of a smaller size Ti^{4+} cation at the Nb site also adds to the dielectric constant. We can anticipate that these external contributions to $\varepsilon_{r'}$ would only make a meaningful impact at higher frequencies. Additionally, it was discovered that the maximum dielectric constant and minimum dielectric loss could be attained at a temperature of Tm equal to 200 ^{o}C for a frequency range of 100 Hz to 100 kHz.

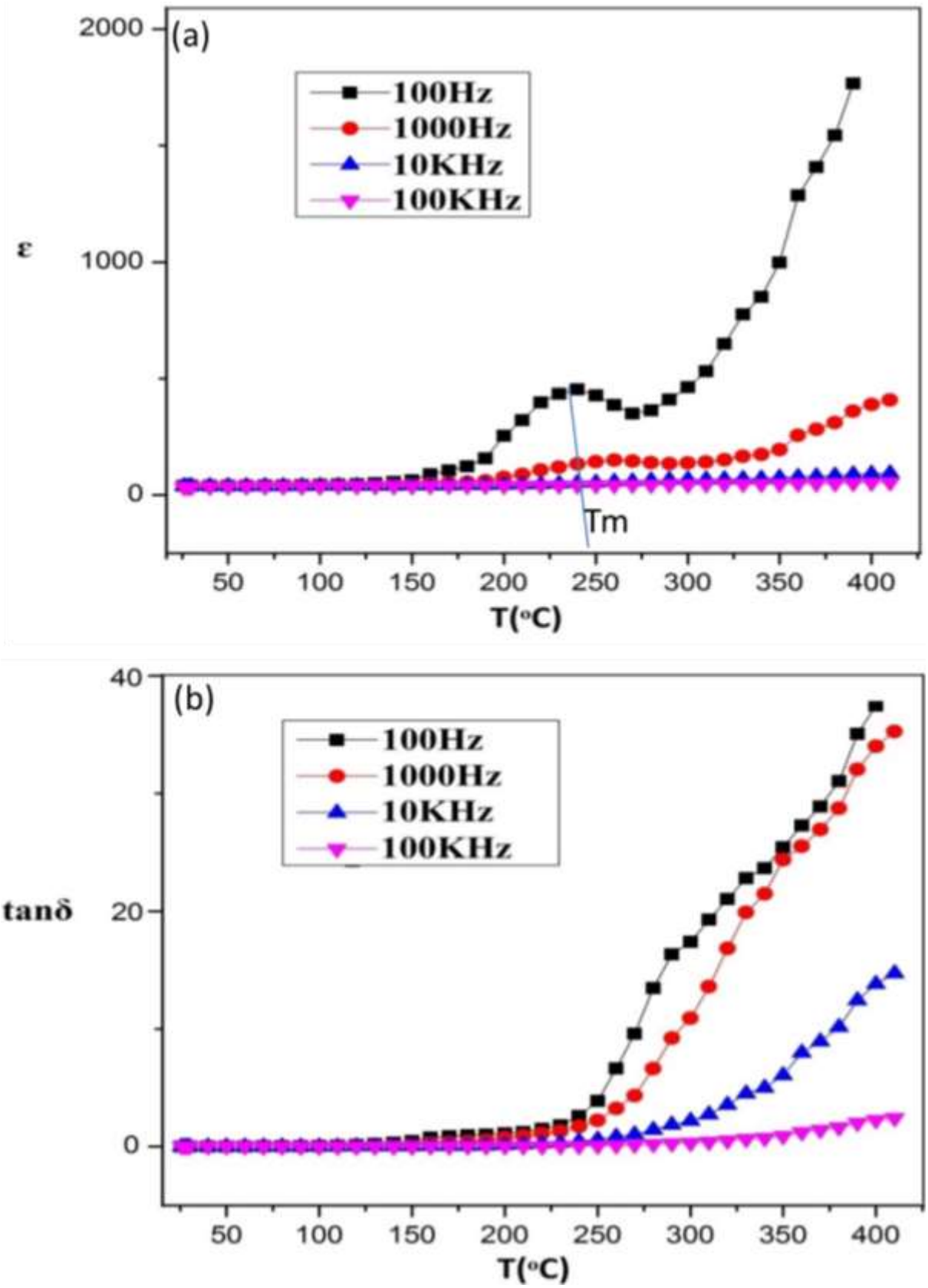

Figure 6.7: (a) Variation of dielectric constant and (b) variation of dielectric loss of $CoNb_2O_6$ pellet at various frequencies with the increase in temperature.

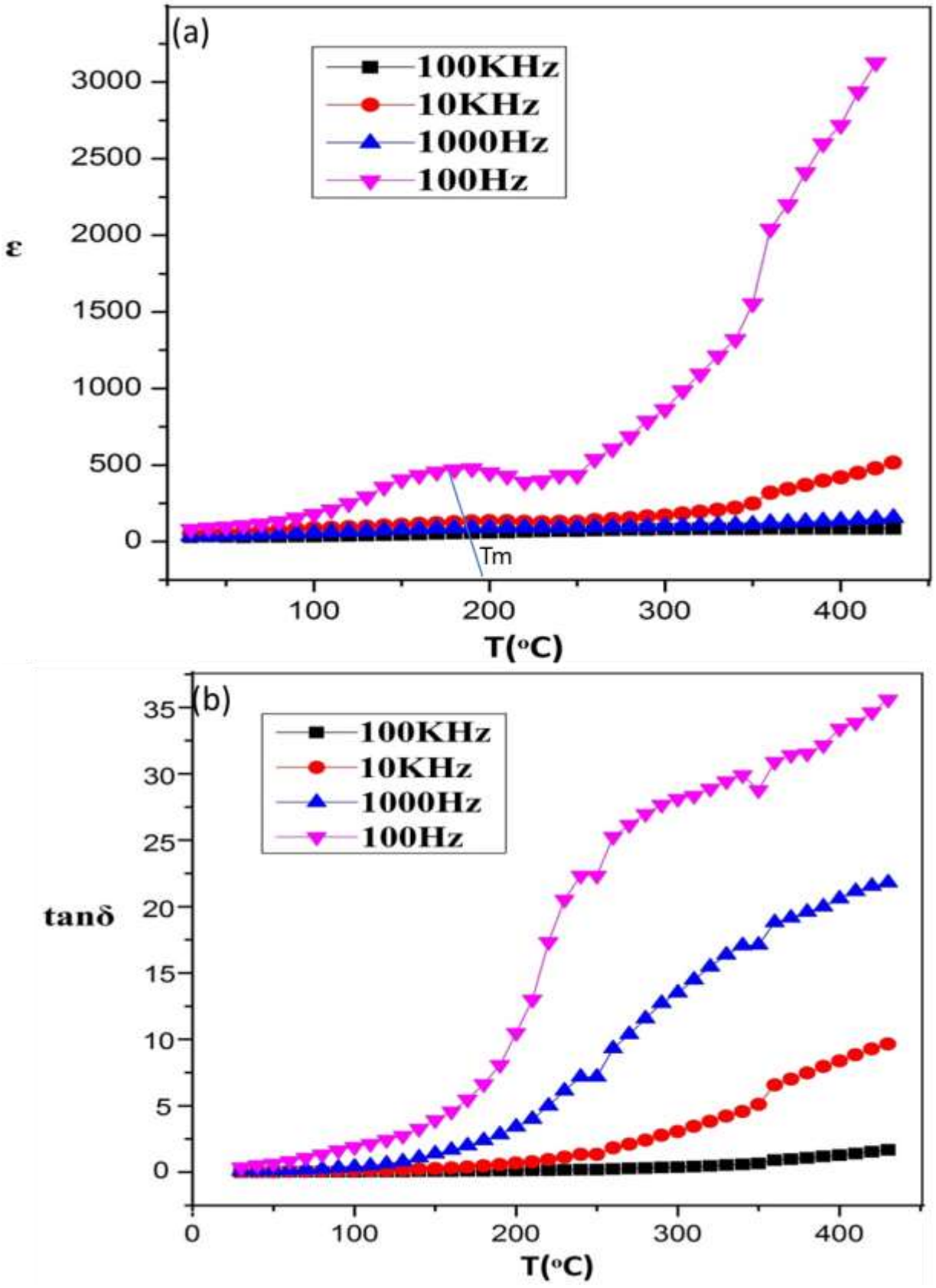

Figure 6.8: (a) Variation of dielectric constant and (b) variation of dielectric loss of $CoNb_{1.95}Ti_{0.05}O_6$ pellet at various frequencies with the increase in temperature.

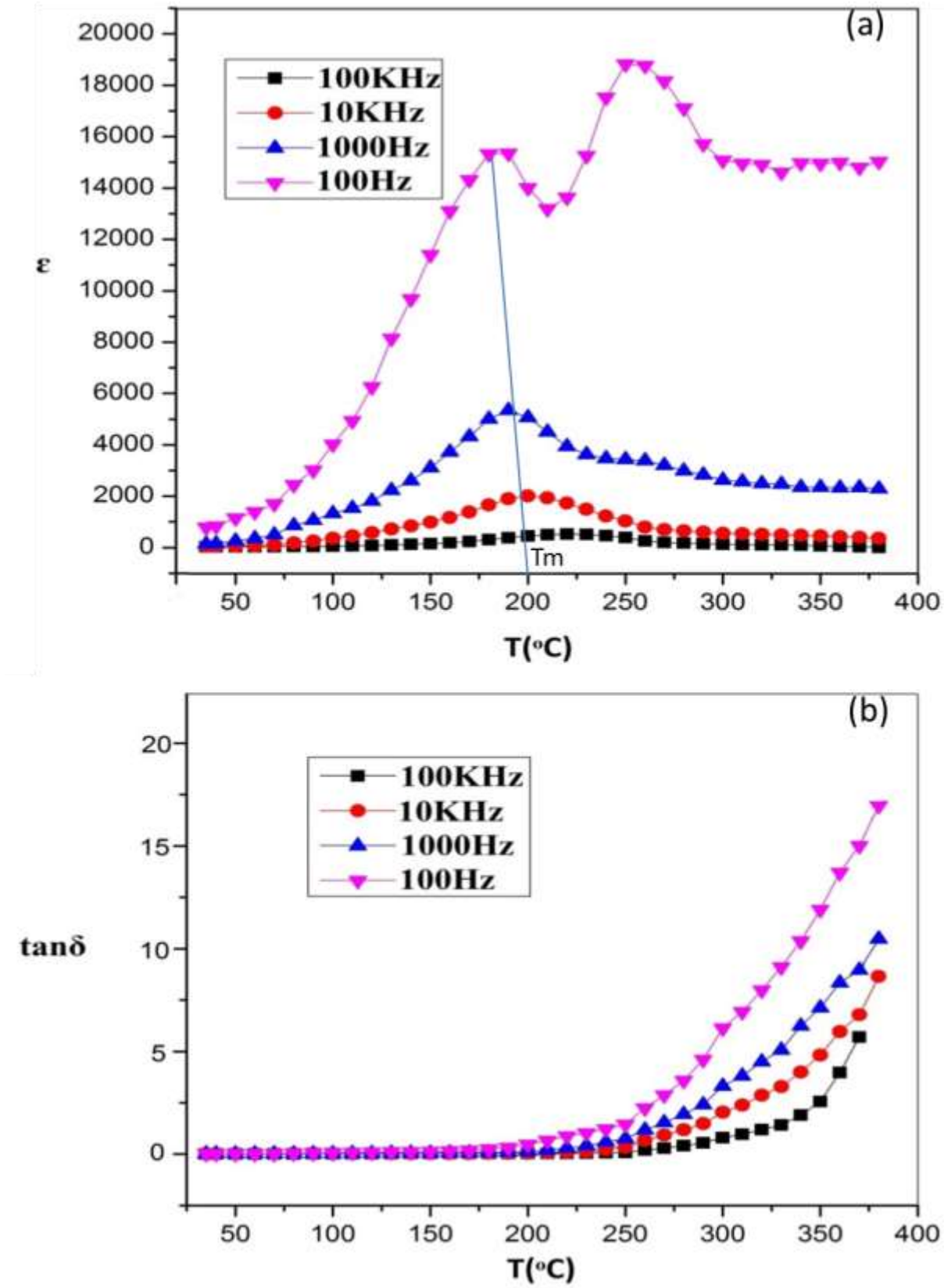

Figure 6.9: (a) Variation of dielectric constant and (b) variation of dielectric loss of $CoNb_{1.9}Ti_{0.1}O_6$ pellet at various frequencies with the increase in temperature.

6.7 P-E Loop Study

Samples $CoNb_2O_6$, $CoNb_{1.95}Ti_{0.05}O_6$, and $CoNb_{1.9}Ti_{0.1}O_6$ exhibit ferroelectricity at room temperature, as illustrated in Figure 6.10 (a, b, and c) respectively. The residual polarization Pr and Vc at 50 Hz frequency are equivalent to 0.05 C/cm^2 and 8*10^{03} V/cm for $CoNb_{1.95}Ti_{0.05}O_6$, and 0.05 C/cm^2 and 10*10^{+03} V/cm for $CoNb_{1.9}Ti_{0.1}O_6$ which are less lossy than the pure $CoNb_2O_6$. The value of Pr and Vc increases at a frequency of 50 Hz when the applied voltage is increased from 10 kV to 45 kV. Ferro-electricity in bulk samples has never been reported before.

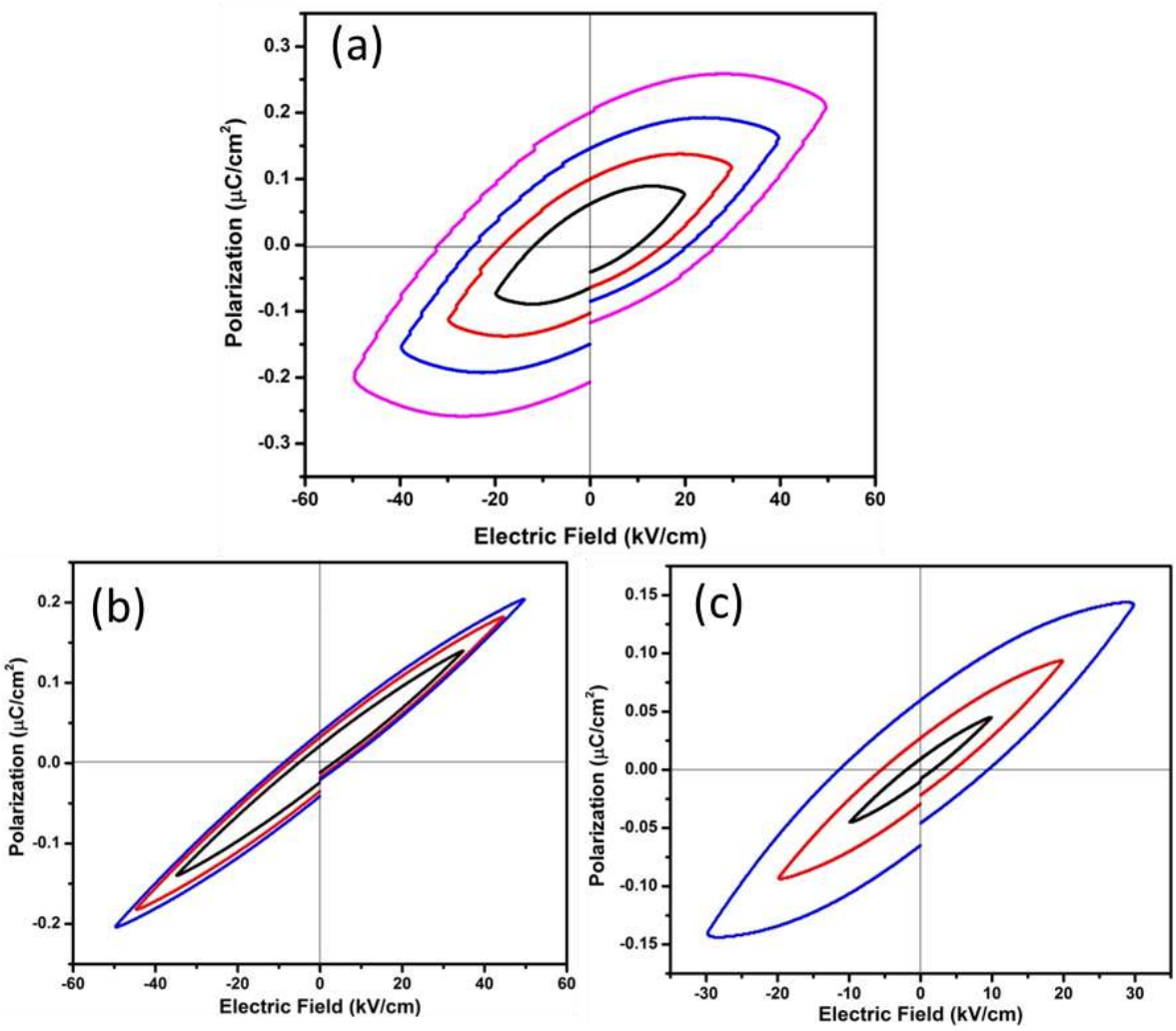

Figure.6.10: A plot of polarization (P) Vs. Electric field (E) for (a) $CoNb_2O_6$, (b) $CoNb_{1.95}Ti_{0.05}O_6$, and (c) $CoNb_{1.9}Ti_{0.1}O_6$ pellets at room temperature and 50 Hz frequency.

6.8 CONCLUSIONS

Single-phase Ti^{4+} ion substituted $CoNb_2O_6$ in the form of $CoNb_{2-x}Ti_xO_6$ is synthesized by a solid-state synthesis route and characterized by powder XRD, SEM, EDX, and XPS studies. Ti^{4+} substitution in the Trirutile $CoNb_2O_6$ lattice enhances the dielectric constant of the material. Similar to well-known PZT type high k Ferroelectrics, Ti^{4+} ion substitution in novel Trirutile $CoNb_2O_6$ lattice resulted in high k dielectricity and overall turned Trirutile into a new family of ferroelectrics as smaller Ti^{4+} can vibrate from its mean position in Trirutile octahedral resulting in net polarization in the octahedral. Also, the entropical effect related to different ionic states of M-O bonds can contribute to the net dipole of trirutile that can affect the dielectric of the materials. Both dielectric constant and dielectric loss were decreasing with increasing frequencies. The dielectric constant (ε_r') for $CoNb_2O_6$ was found to be 500, $CoNb_{1.95}Ti_{0.05}O_6$ is 700 and $CoNb_{1.9}Ti_{0.1}O_6$ is 14000 respectively at 100 Hz frequency at 200^oC and then decreases, clearly shows relaxor type behavior. Samples also exhibit ferroelectric behavior with remnant polarization Pr and Vc at 50Hz frequency equal to 0.05 $\mu C/cm^2$ and $8*10^{+03}$V/cm for $CoNb_{1.95}Ti_{0.05}O_6$ and 0.05 $\mu C/cm^2$ and $10*10^{+03}$V/cm for $CoNb_{1.9}Ti_{0.1}O_6$.

REFERENCES

1. J.F. Scott, A. Schilling, S.E. Rowley, J.M. Gregg, Some current problems in perovskite nano-ferroelectrics and multiferroics: kinetically-limited systems of finite lateral size, Sci. Tech. Adv. Mater., 16 (2015), Article 036001.
2. W. Känzig, Ferroelectrics and Antiferroelectrics, Solid State Physics 4 (Academic Press, New York, 1957), ISBN 0-12-607704-5.
3. M. Lines and A. "Glass, Principles and Applications of Ferroelectrics and Related Materials" (Clarendon Press, Oxford, 1979), ISBN 0-19-851286-4,
4. W. Eerenstein, N. D. Mathur and J. F. Scott, Multiferroic and magnetoelectric materials, Nature 442, 759 (2006).
5. C. W. Nan, M. I. Bichurin, S. X. Dong, D. Viehland and G. Srinivasan, Multiferroic magnetoelectric composites: Historical perspective, status, and future directions, J. Appl. Phys. 103, 031101 (2008).
6. C. A. F. Vaz, J. Homan, C. H. Ahn and R. Ramesh, Magnetoelectric coupling effects in multiferroic complex oxide composite structures, Adv. Mater. 22, 2900 (2010).
7. L W Martin, S P Crane, Y-H Chu, M B Holcomb, M Gajek, M Huijben, C-H Yang, N Balke and R Ramesh, Multiferroics and magnetoelectrics: thin films and nanostructures, J. Phys.: Condens. Matter. (2008). 20, 434220
8. P. K. Amiri and K. L. Wang, Voltage-controlled magnetic anisotropy in spintronic devices, Spin 2012 2 (03), 1240002.